

Star Cluster Ecology: VII The evolution of young dense star clusters containing primordial binaries

Simon F. Portegies Zwart,^{1,2} Stephen L. W. McMillan³ Junichiro Makino⁴

^{1,2} *Astronomical Institute 'Anton Pannekoek', University of Amsterdam, Kruislaan 403, 1098SJ Amsterdam, the Netherlands,
Section Computational Science, University of Amsterdam, Kruislaan 403, 1098SJ Amsterdam, the Netherlands*

³ *Department of Physics, Drexel University, Philadelphia, PA 19104, USA*

⁴ *Department of Astronomy, University of Tokyo, Tokyo 113, Japan*

12 June 2018

ABSTRACT

We study the first ~ 100 Myr of the evolution of isolated star clusters initially containing 144179 stars, including 13107 (10%) primordial hard binaries. Our calculations include the effects of both stellar and binary evolution. Gravitational interactions among the stars are computed by direct N-body integration using high precision GRAPE-6 hardware. The evolution of the core radii and central concentrations of our simulated clusters are compared with the observed sample of young ($\lesssim 100$ Myr) star clusters in the large Magellanic cloud. Even though our simulations start with a rich population of primordial binaries, core collapse during the early phase of the cluster evolution is not prevented. Throughout the simulations, the fraction of binaries remains roughly constant ($\sim 10\%$). Due to the effects of mass segregation the mass function of intermediate-mass main-sequence stars becomes as flat as $\alpha = -1.8$ in the central part of the cluster (where the initial Salpeter mass function had $\alpha = -2.35$). About 6–12% of the neutron stars were retained in our simulations; the fraction of retained black holes is 40–70%. In each simulation about three neutron stars become members of close binaries with a main-sequence companion. Such a binary will eventually become an x-ray binary, when the main-sequence star starts to fill its Roche lobe. Black holes are found more frequently in binaries; in each simulated cluster we find ~ 11 potential x-ray binaries containing a black hole. Binaries consisting of two white dwarfs are quite common, but few (20–30) are sufficiently close that they will merge within a Hubble time due to the emission of gravitational radiation. Clusters with shorter relaxation times tend to produce fewer merging white dwarf binaries. The white dwarf binaries that do merge are all sufficiently massive to produce a type Ia supernova. The densest cluster produces about twice as many blue stragglers as a field population containing the same number of binaries, and these blue stragglers are more massive, bluer and brighter than in less dense clusters.

1 INTRODUCTION

High-quality ground- and space-based observations over the past two decades have revealed the existence of numerous young, dense star clusters in our Galaxy and beyond. Examples include (1) the Arches (Figer et al. 2002; Stolte et al. 2005) and Quintuplet (Figer et al. 1999) systems in the Galactic center (Genzel et al. 2003; Ghez et al. 2003); (2) the rich clusters NGC 3603 (Moffat et al. 1994, 2004) and Westerlund 1 (Piatti et al. 1998; Clark et al. 2005) in the Galactic disk; (3) the R136 (Massey & Hunter 1998) system and other young clusters in the Large Magellanic Cloud (LMC) (Mackey & Gilmore 2003); (4) an increasing number of young star clusters in nearby starburst systems such as the Antennae and a newly discovered cluster (Bica et al. 2003a,b; Figer et al. 2006).

These systems are of great interest for a number of

reasons. First, as both observations and simulation techniques continue to improve, evolutionary studies of model systems allow us to probe the dynamical state of observed clusters, and may offer key insights into the conditions under which star clusters are born. Second, these dense clusters are likely to be the sites of complex physical phenomena, such as stellar collisions and mergers (Portegies Zwart et al. 1999; Portegies Zwart & McMillan 2002; Gürkan et al. 2004; Freitag et al. 2006), placing them at the interface of stellar dynamics, stellar and binary evolution, and stellar hydrodynamics. Partly as a result of this overlap of traditionally distinct astrophysical disciplines, the past few years have seen an upsurge in interest in modeling dense stellar systems, which pose significant theoretical and technical challenges to researchers (Hut et al. 2003;

Sills et al. 2003).¹ Finally, since such clusters may plausibly be the progenitors of globular-cluster like systems, the studies presented here also offer valuable clues to the early evolution of the globular cluster systems observed in many galaxies. The early evolutionary conditions considered here may also have important consequences for the present-day content of globulars.

In performing simulations of young star clusters we run into an immediate problem. The initial conditions of these systems have been actively debated for many years, but no consensus has been reached. Models of star formation are as yet insufficiently advanced to provide definitive predictions of initial structure for large systems (Klessen 2001; Padoan & Nordlund 2002; Bate & Bonnell 2005), and we cannot simply run an observed cluster backwards in time, even if its parameters were all known to arbitrary accuracy. Rather, we start with a poorly determined but plausible initial state, evolve it forward in time, then attempt to match observable properties of our model cluster with actual clusters in the universe to assess the reasonableness of our initial choice.

In this study we simulate young (age $\lesssim 100$ Myr) star clusters by integrating the equations of motion of all stars and binaries. We use the Starlab environment (Portegies Zwart et al 2001), which acquires its greatest speed on the GRAPE-6 special-purpose computer (GRAvity PipE, Makino et al 1997; 2003). The calculations presented here were performed on the GRAPE hardware at the University of Tokyo, the MoDeStA² platform in Amsterdam, and the GRAPE-6 system at Drexel University. Both stellar and binary evolution are included self-consistently in our models.

2 SIMULATIONS

We focus on four basic cluster simulations (#1–4), with initial conditions summarized in Table 1. For each realization, one full calculation from zero age to about 100 Myr was performed; for simulations #1 and #2 one additional realization was computed. As discussed in more detail below, these simulations differ only in the choice of length (and hence time) scales, effectively exploring the dependence of the evolution on the ratio of the cluster relaxation time to the (fixed) time scale for stellar evolution. In each case, further simulations have been performed to test the sensitivity of portions of the evolution to different choices of physical parameters, such as the suppression of binary heating or stellar mass loss.

The model clusters are initialized by selecting the number of stars, the stellar mass function, the binary fraction and the distribution of binary orbital elements, and the density profile. For our most compact model (simulation #1) we adopt the initial conditions derived by Portegies Zwart et al. (2004) to mimic the 7–12 Myr old star cluster MGG-11 in the starburst galaxy M82, which was observed in detail by McCrady et al. (2003). In this paper, however, we extend the evolution of that model to about 100 Myr. The initial half-mass relaxation time of simulation #1 is 80 Myr; the other simulations are performed with larger cluster radii, resulting in longer relaxation times.

¹ See for example <http://manybody.org/modest>.

² See <http://modesta.science.uva.nl>

We summarize here the choice of initial conditions for simulation #1. We select $N = 131072$ (128k) stars from a King (1966) $W_0 = 12$ density distribution (see Portegies Zwart et al. 2004). For simplicity, stellar masses are drawn from a Salpeter initial mass function ($\alpha = -2.35$) between $1 M_\odot$ and $100 M_\odot$. The lower limit is set by the recent indications that mass functions in such young and massive star clusters may be truncated below about $1 M_\odot$ at least for several star clusters including knot F in M82 (Smith & Gallagher 2001), MGG-11 in the same galaxy (McCrady et al. 2003), and the Arches cluster in the Galactic center (Stolte et al. 2005). The mass function also appears to be truncated at the upper end, at around 100 – $150 M_\odot$ (Weidner & Kroupa 2004; Figer 2005). Between these limits the power-law can be described adequately by the Salpeter slope (Salpeter 1955; Kroupa 2001).

The most widely used mass functions, such as Kroupa (2001), peak around $0.5 M_\odot$. If we had included the low-mass stars from these distributions, the total number of stars in our simulations would have increased by about a factor of 2.6, while the total mass would have increased by about 30%. The increased relaxation time due to this change might have a significant effect on the long-term dynamical evolution of the simulated clusters, but during the first ~ 100 Myr the effect is expected to be small, since the early evolution of these clusters is dominated by the massive stars. We therefore expect that the neglect of low-mass ($< 1 M_\odot$) stars does not profoundly affect our results.

There is no primordial mass segregation—that is, a star’s initial position is uncorrelated with its mass. Ten percent of the stars are selected randomly as binary primaries and are provided with a companion (secondary) star with mass distributed uniformly between $1 M_\odot$ and the mass of the primary. The total mass of the cluster is then $M \simeq 433000 M_\odot$. Binary parameters are determined by choosing a binding energy and orbital eccentricity. The latter is taken randomly from a thermal distribution [$f(e) = 2e$], whereas the binding energy is taken randomly (uniform in $\log E$) between $E = 10 kT$ (corresponding to a separation of about $1000 R_\odot$) and maximum binding energy such that the corresponding distance between the two stars at pericenter exceeds the sum of their radii. (The energy scale kT is defined by the condition that the total stellar kinetic energy of the system, excluding internal binary motion, is $\frac{3}{2} N kT$.)

For the other simulations (#2–4), we adopt the same realization of the initial stellar masses, positions and velocities (in virial N-body units [Heggie & Mathieu 1986]), but with a different size and time scaling for the stellar evolution, such that the half-mass two-body relaxation time (t_{rh}) for simulations #2, #3, and #4 are, respectively, 4, 16, and 64 times that for simulation #1. The binary populations in these simulations therefore have larger maximum orbital separations in clusters with longer relaxation times, because the adopted minimum binding energy of $10 kT$ shifts to smaller physical values. Simulations #2, #3 and #4 have maximum orbital separations of roughly $2000 R_\odot$, $5000 R_\odot$ and $10^4 R_\odot$, respectively.

After initialization we solve the equations of motion for the stars in the cluster potential using the Starlab **kira** integrator, simultaneously calculating the evolution of the stars and binaries. The stellar evolution model adopted is based on Eggleton, Fitchett & Tout (1989), and the binaries

Table 1. Parameters of the four simulations. In each case the total mass is $M = 433209 M_{\odot}$, the number of stars is 131072 (128k), the core mass is $M_{\text{core}} = 0.00298M = 1282 M_{\odot}$, and the core number is $N_{\text{core}} = 360$. The runs differ only in the choice of virial radius, and therefore in the density within the virial radius (ρ_{vir}). All contain an initial binary fraction of 10%, with orbital parameters as described in the text.

Simulation	r_{vir} [pc]	r_{core} [pc]	ρ_{vir} [M_{\odot}/pc^3]	t_{ch} [Myr]	t_{rh} [Myr]	t_{cc}
#1	1.27	0.010	40100	0.032	80	40
#2	3.2	0.026	2500	0.129	320	77
#3	8.1	0.066	155	0.516	1300	$\gtrsim 100$
#4	20	0.162	10.2	2.067	5100	$\gtrsim 100$

are evolved using **SeBa** (Portegies Zwart & Verbunt 1996; Portegies Zwart & Yungelson 1998). We ignore any external tidal field, but stars are removed from the simulation when they reach more than 60 initial half-mass radii from the density center of the cluster. The neglect of the tidal field limits the validity of our results to relatively isolated clusters like NGC 3603 and Westerlund 1. These initial conditions may also be applicable to the star clusters in the LMC, like R 136, as the low density and irregular shape of this galaxy imposes only a shallow background potential on these clusters. All calculations are continued to an age of about 100 Myr.

During the integration of simulation #2, total energy is conserved on average to better than one part in $10^{7.1 \pm 1.7}$ per crossing time, with a total fractional difference between the final and initial energies (corrected for mass loss and other explicitly non-conservative events, such as supernova explosions or stellar collisions) of $\sim 10^{-4}$. For the other runs the energy conservation is at least an order of magnitude better. Simulations #3 and #4 have better energy conservation because they are larger clusters for which fewer integration timesteps had to be taken and during which fewer strong dynamical multibody encounters occurred. Simulation #1, although more compact than #2, exhibited an early phase of core collapse during which a collision runaway occurred (see Portegies Zwart et al. (2004)). Such events are generally easier for the N -body integrator to handle, compared to the many strong dynamical multibody interactions in simulation #2. In addition we performed a second simulations with the same realization #1, this second simulation we call #1R. The main difference between simulation #1 and #1R is the treatment of supernovae in the massive collision runaways occurring in those simulations. In simulation #1 the very massive star collapses to a $39 M_{\odot}$ black hole, losing about $1193 M_{\odot}$ in the supernova, whereas in simulation #1R the same star collapses to a $1232 M_{\odot}$ black hole without losing any mass in the supernova explosion.

3 RESULTS

In this section we discuss the early evolution of star clusters #1–4. We focus on the observational consequences for these simulations, discussing the stellar and binary populations.

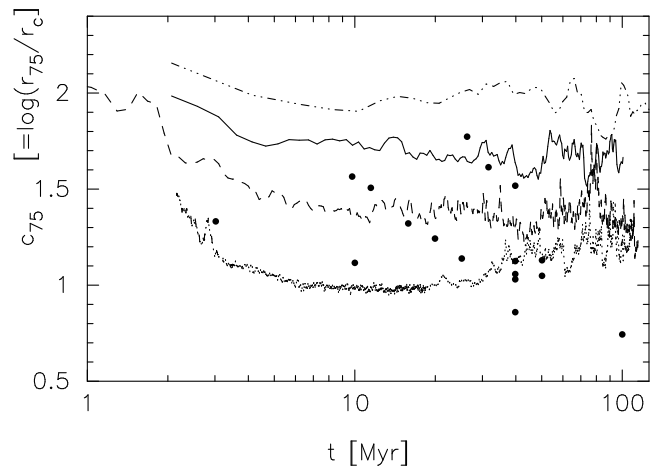


Figure 1. Evolution of the concentration c_{75} [defined here as $\log_{10}(r_{75}/r_{\text{core}})$] for the simulated clusters #1 (dotted curve), #2 (dashes), #3 (solid) and #4 (dash-3-dotted curve). For comparison we show (bullets) the measured concentrations for the young LMC clusters from Mackay & Gilmore (2003).

3.1 Evolution of cluster structural parameters

Figures 1 and 2 show the evolution of the central concentration and core radii of our simulations. In addition, we overplot as bullets the structure measurements for the LMC star clusters reported by Mackay & Gilmore (2003). Those authors list a total of 16 LMC clusters younger than 100 Myr, and 25 younger than 1 Gyr. They provide some structural data, although not directly related to the commonly used concentration parameter c , defined as $c = \log r_{\text{tide}}/r_c$. Since our simulation models are isolated, we also have opted for a slightly modified definition of the concentration: we use the 75% Lagrangian radius (r_{75}) instead of the tidal radius in the definition, and write $c_{75} \equiv \log r_{75}/r_c$. Mackay & Gilmore (2003) do not measure the tidal radii of their clusters, but from their structure parameters we can readily estimate the 75% Lagrangian radii.

Figure 1 compares the concentration parameter (c_{75}) derived from observations with the results of our simulations #1–4, which generally bracket the observed parameters except at very low concentrations around 100 Myr. The low concentrations of these older clusters may be due to a rather flat initial mass function which drives a more dramatic expansion even at later times, by stellar-wind mass loss (Takahashi & Portegies Zwart 2000), by dynamical heating due to the presence of a large number of stellar mass black

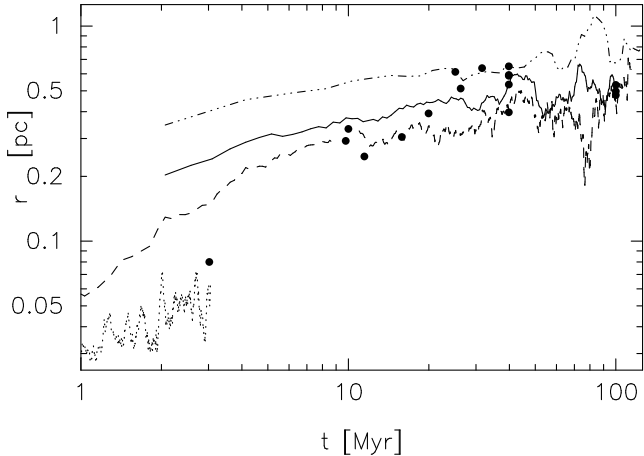


Figure 2. Measurement for the core radius (estimated as $0.25r_c$, with r_c taken from Mackay & Gilmore (2003)) for the clusters listed in Mackay & Gilmore (2003). To guide the eye we plot the evolution of the core radius of model #1 (dotted curve), #2 (dashed line), #3 (solid curve) and #4 (dash-3-dotted curve). Note the unusually small core radius of the star cluster R136 (leftmost point) which actually lies on the evolution of the core radius for simulation #1 (not shown here). The curve for simulation #1 is only shown for the first few Myr, as at later times it becomes quite noisy and runs into the curve for simulation #2, making them both hard to distinguish.

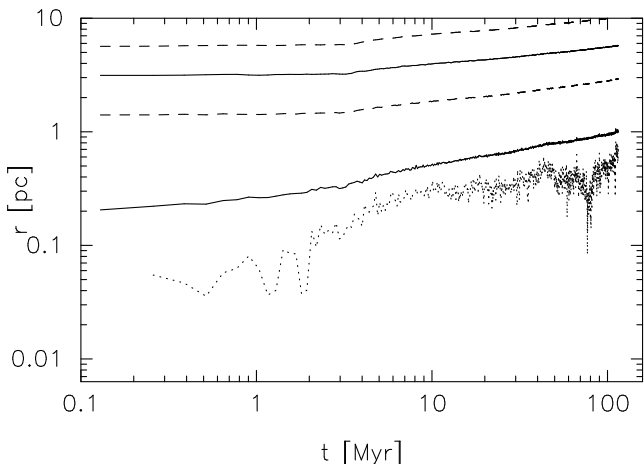


Figure 3. Evolution of the core radius (dotted curves), 5% Lagrangian radius (lower solid), 25% (lower dashed line), half mass radius (upper solid) and 75% Lagrangian radii for simulation #2.

holes of the cluster (Merritt et al. 2004) or by a (much) larger population of primordial binaries (Heggie et al. 2006; Trenti et al. 2006) than we assumed here. Figure 2 compares the evolution of the core radii in simulations #2, #3 and #4 with the core radii of the clusters in the Mackay & Gilmore sample. The core radii in the LMC sample are determined by fitting the observed intensity profiles with 2-parameter King (1966) models, the parameters being half-mass radius and concentration. The core radius in these models is generally about a factor of four larger than that defined by theorists.³

³ The observer's core radius is traditionally where the surface

We correct for this discrepancy by dividing the core radii provided by Mackay & Gilmore by a factor of four.

Except for the star cluster R136 (the central cluster of NGC 2070; leftmost point) the observed core radii appear to be quite consistent with the core evolution of simulations #2–4. The core radius of R136 is consistent with that of simulation #1 (partially shown in Figure 2) .

3.2 Evolution of the mass function

All simulations started with a Salpeter (power-law with exponent $\alpha = -2.35$) mass function. The global mass function changes with time due to stellar evolution and selective evaporation driven by the dynamical evolution of the cluster. The mass function also varies locally due to mass segregation. To quantify the global and local changes in the stellar mass function, we first select those stars which remain on the main sequence during the entire period studied. The turn-off mass at 100 Myr in our stellar evolution model is about $4.6 M_\odot$. By restricting ourselves to main-sequence stars in the rather narrow mass range of 1 to $4.6 M_\odot$ we guarantee that the mass function is not affected by blue stragglers, giants or stellar remnants, although some contamination from dormant blue stragglers cannot be avoided (see § 3.4).

Figure 4 shows the evolution of the cluster mass function exponent between 1 and $4.6 M_\odot$ for simulation #1. The exponent was calculated using a least-squares fit to the binned (100 bins) mass data. From top to bottom, the curves present the mass function exponent (i) within the 10% Lagrangian radius (together with an analytic fit, as described below), (ii) within the 25% Lagrangian radius, (iii) within the half-mass radius (50% Lagrangian radius), (iv) for the entire cluster, (v) outside the half-mass radius, (vi) outside the 75% Lagrangian radius, and (vii) outside the 90% Lagrangian radius. The global mass function (lower solid curve) steepens slightly with time, from $\alpha \simeq -2.41$ at birth to about $\alpha \simeq -2.43$ at an age of 100 Myr. Note that the value of the mass function exponent is not -2.35 because of the presence of binaries. The mass function for the inner 10% of the stars (upper dash-3-dotted curve in Figure 4) is most strongly affected by mass segregation.

The slight steepening of the global main-sequence mass function is the result of dynamical activity in the cluster center, which tends to eject relatively high mass stars from the cluster more frequently than lower mass stars, simply because the latter are not as abundant in the cluster core, and hence do not participate so frequently in strong dynamical encounters. Thus the change in the global mass function is driven mainly by dynamical encounters in the cluster core, and not by selective evaporation (but see Lamers et al. (2006)). This is in part because of our neglect of a global tidal field. At about 60 Myr the global mass function stops changing because the white dwarfs formed subsequently are

brightness drops by a factor of two. The “continuum” theorist's core radius is defined in terms of the central density and velocity dispersion, not from the density variation, although the falloff is implicit in the solution to Poisson's equation. The N-body theorist's core radius is something different again, defined in terms of local density from the criterion proposed by Casertano & Hut (1985). Remarkably, they all seem to have something to do with one another.

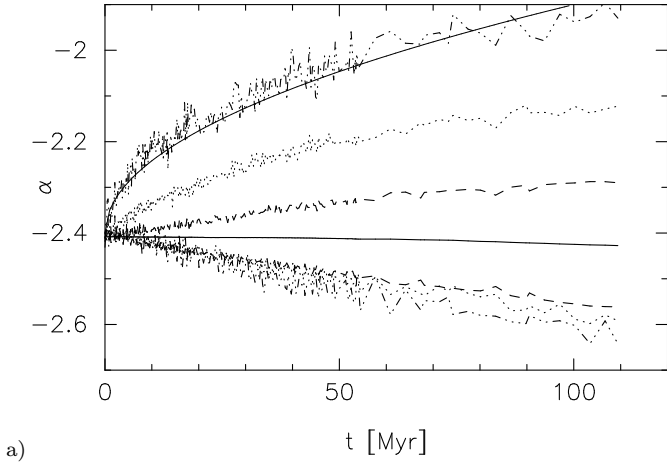
a) t [Myr]

Figure 4. Evolution of the power-law exponent α of the mass function for simulation #1 for main-sequence stars of masses between 1 and $4.6 M_{\odot}$. The solid almost horizontal curve represents the entire cluster. The curves above it (flatter mass function) give the value of the power-law slope to the mass function of the stars which are *inside* the 50% (dashes), 25% (dotted line) and 10% (dash-3-dotted line) Lagrangian radii. The curves below the solid curve in the middle (steeper mass function) give the value of the power-law slope to the mass function of the stars which are *outside* the 50%, 25% and 10% Lagrangian radii. The thin solid curve through the upper dash-3-dotted curve (mass function of the stars within the 10% Lagrangian radius) is calculated using $\alpha \propto \sqrt{t}$ (see text). Similar expressions fit the lower curves. (Note that after 55 Myr we increased the output time interval from 1 Myr to 5 Myr).

comparable in mass to the least massive main-sequence stars in the simulation, and compete with them dynamically.

The mass functions for the stars in the outer parts of the cluster become steeper with time, with power-law exponents ranging from $\alpha \simeq -2.56$ for the outermost 50% to $\alpha \simeq -2.64$ for the outer 10% Lagrangian radius in simulation #1. The mass functions in the inner parts of the cluster become flatter with time. Within the half-mass radius the mass function flattens to $\alpha \simeq -2.3$ in about 100 Myr; for the inner 10% Lagrangian radius the mass function flattens to $\alpha \simeq -1.9$. The other simulations had considerably smaller changes in the global mass function.

We fit the variation in the mass function exponent in the inner part of the cluster by

$$\alpha(t) = \alpha(0) + \left(\frac{t}{\tau}\right)^{0.5} \quad (1)$$

(Merritt et al. 2004). Here $\alpha(0)$ is the initial power-law slope and τ is a constant. For stars within the inner 10%, 25%, and 50% of the simulation (top three dashed/dotted curves in Figure 4), the best-fitting values of τ are $\sim 5t_{\text{rh}}$, $15t_{\text{rh}}$, and $130t_{\text{rh}}$, respectively. The fit for the inner 10% Lagrangian radius is presented in Figure 4 as the upper thin solid curve. The mass functions in the other runs vary similarly, with the same scaling ($\propto t_{\text{rh}}$) but larger coefficients.

3.3 Evolution of the stellar population

As the cluster ages, main sequence stars turn into giants, which then evolve into stellar remnants. This is illustrated

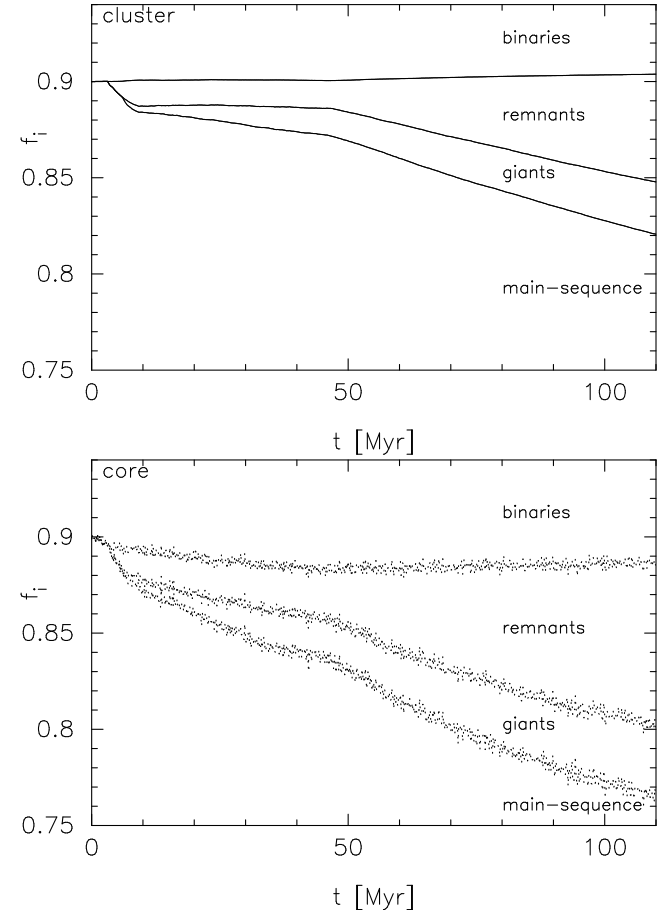


Figure 5. Stellar content of simulation #2 as a function of time. We distinguish here between main-sequence stars, giants, remnants (single white dwarfs, neutron stars and black holes) and binaries. The regions between the various lines indicate the fraction of each category of object, as is indicated for the solid curves to the right of the figure. The **top panel** give these branching ratios for the entire cluster (in solid curves), while the dotted lines in the **bottom panel** show the branching ratios for the inner 10% Lagrangian radius. The various stellar groups are represented in the same order, but due to the different evolution in the cluster interior they are shifted with respect to the solid curves.

in Figure 5, which shows the stellar content of simulation #2. Here we distinguish between binaries (top part of the diagrams) and single stars (bottom part). For the single stars, we make a further division into main sequence stars, giants and compact objects. The total is normalized to unity so that the diagram gives the relative fraction of each type of object as a function of time. The solid curves (top panel) represent the population of the entire star cluster; dotted curves (bottom panel) present the same population information for the innermost 10% of the system.

Initially, the cluster contains binaries and main-sequence stars, but the composition changes as stars evolve, and by an age of about 10 Myr a significant population of giants and stellar remnants is established. Between 10 and ~ 50 Myr the fraction of giants gradually increases at the cost of the main-sequence stars, while the fraction of stellar remnants hardly changes. The main reason for the constancy of the fraction of stellar remnants is that the neu-

tron stars, which are born during this time interval, tend to be ejected from the cluster upon formation (see § 3.7 below). After about 50 Myr the relative fractions of giants and remnants increase more rapidly than before, primarily because of the formation of white dwarfs (see also Figure 11).

The relative fraction of binaries in the inner parts of the cluster (top curve in the bottom frame of Figure 5) is larger than for the cluster overall, and the same is true for remnants and giants. The reason for this is that these objects are all more massive than the average main-sequence star, and therefore sink to the center by mass segregation.

One of the most interesting features in Figure 5 is the roughly constant proportion of binaries. The total binary fraction drops by only about 10% percent during the 100 Myr of the evolution. For the other models, the binary fraction falls from its initial value of 10% to 9.1% for model #2, 8.9% for model #3 and to 9.0% for model #4. This result is consistent with the findings of Shara & Hurley (2006), who observed only a slight decay in the initial binary fraction in their simulations of the cores of dense star clusters.

3.4 Characteristics of the blue straggler population

All the stars in our simulated clusters are born on the zero-age main-sequence. The normal evolution of a star may be altered by mass transfer from a more massive Roche-lobe filling companion, or by collisions with other stars. Mass gained from a companion causes an accretor to become more massive, and may also refresh the nuclear fuel in the stellar interior by mixing central helium with fresh hydrogen. Internal mixing tends to rewind the nuclear clock of the star. A physical collision between two main sequence stars may have a similar effect (Sills & Lombardi 1997; Sills et al. 2001; Lombardi et al. 2002; Sills et al. 2005). Either effect may “rewind” the star’s nuclear clock, and such rejuvenated stars can appear on a Hertzsprung-Russell diagram as blue stragglers. For definiteness, we identify a blue straggler as a main-sequence star with mass larger than the turn-off mass at the current cluster age.

In each simulation an appreciable number of blue stragglers formed, mostly through mass transfer in close binaries. Collisions between main-sequence stars are rare, except in simulations #1R and #1, where they give rise to a collision runaway. Run #1R in its first 12 Myr is identical to one of the simulations described in Portegies Zwart et al. (2004). In such dense systems, repeated collisions can result in an unusually massive blue straggler (Hurley et al. 2001; Lombardi et al. 2003) within the first few million years. A collision between a main sequence star and an evolved (sub-giant) star generally does not result in the formation of a blue straggler; a bright giant is a more common outcome (Portegies Zwart et al. 1997).

Figure 6 presents the evolution of the total numbers of blue stragglers in simulations #1 through #4. The number of blue stragglers in each simulation increases steadily with time. Up to an age of about 50 Myr, the number increases at a similar rate in each of the simulations. After ~ 50 Myr, the number in the two shallower clusters (#3 and #4) continues to increase, but at a lower rate. The growth rate of the number of blue stragglers in these models is consistent

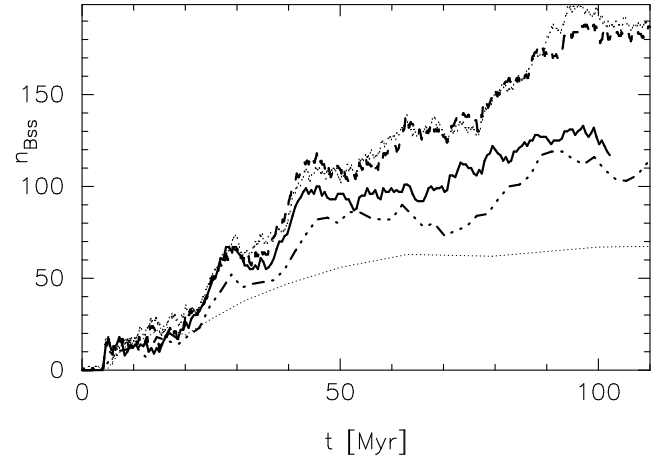


Figure 6. Evolution of the number of blue stragglers in simulations #1 (dotted curve), #2 (dashes), #3 (solid curve), #4 (dash-dot curve). The results of the binary population synthesis of model A17 by Pols & Marinus (1994) are presented as the lower thin dotted line.

with expectations based on the binary population synthesis calculations of Pols & Marinus (1994).

In the population synthesis study of Pols & Marinus (1994), gravitational interactions with other cluster stars were ignored. In their model A17 they adopted a similar mass function to ours, but with a minimum mass of $1.47 M_{\odot}$ instead of our minimum mass of $1.0 M_{\odot}$ (see § 2), and they included a slightly wider binaries than in our simulation #4. They simulated 17000 objects with a 75% binary fraction, resulting in 12 750 binaries, comparable to the 13 107 binaries in our models #1 to #4. The differences in initial conditions are expected to increase the number of blue stragglers in our simulation #4 by at most a factor of two compared to model A17 of Pols & Marinus (1994). In Figure 6 we reproduce the evolution of the number of blue stragglers in their model A17. The results of our simulation #4 (dash-dot curve) is consistent with their model A17. We continued simulation #4 to an age of about 400 Myr to confirm that also at later time ($t > 100$ Myr) the number of blue stragglers in this simulation is consistent with the results of simulation A17.

To allow comparison of the characteristics of the blue stragglers at different times we consider the quantity m/m_{to} , the mass of a blue straggler normalized to the instantaneous turn-off mass. Figure 7 presents the cumulative distribution of m/m_{to} at various moments in time during the evolution of the densest cluster, simulation #1. In this simulation, only $\lesssim 20\%$ of the blue stragglers have masses less than 40% above the turn-off; most have $m/m_{\text{to}} \sim 1.4 - 1.7$. The main difference between these curves is simply the numbers of blue stragglers—the shapes of the normalized distributions are almost indistinguishable.

In Figure 8 we show the cumulative distribution, at an age of 100 Myr, of L/L_{to} , the blue straggler luminosity relative to the luminosity of a main-sequence star at the turn-off. These distributions change only slightly with time. Most striking in Figure 8 are the run-to-run variations: a decrease in cluster density causes the median blue straggler mass to drop gradually from $m/m_{\text{to}} \simeq 1.6$ for simulation #1 to

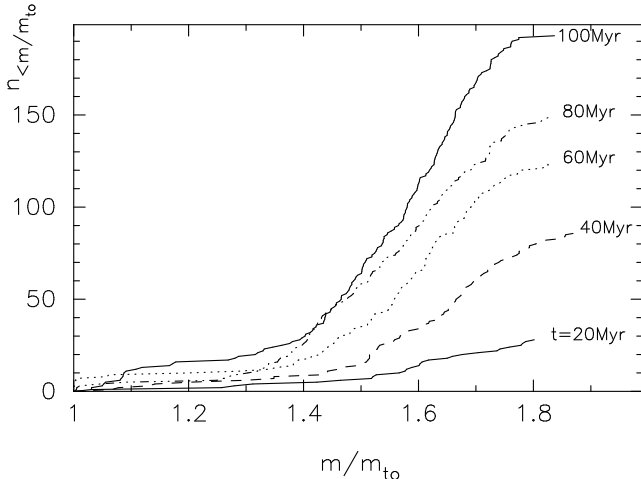


Figure 7. Cumulative distribution of masses above the turn-off mass for blue stragglers at various instants during simulation #1. The mass at the turn off is $m_{\text{to}} \simeq 10.76 M_{\odot}$ at an age of 20 Myr (lower solid line in Figure 7), $m_{\text{to}} \simeq 7.29 M_{\odot}$ at 40 Myr (dashes), $6.03 M_{\odot}$ at 60 Myr (dots), $5.15 M_{\odot}$ at 80 Myr (dash-3dots) and $4.63 M_{\odot}$ at 100 Myr (top solid curve).

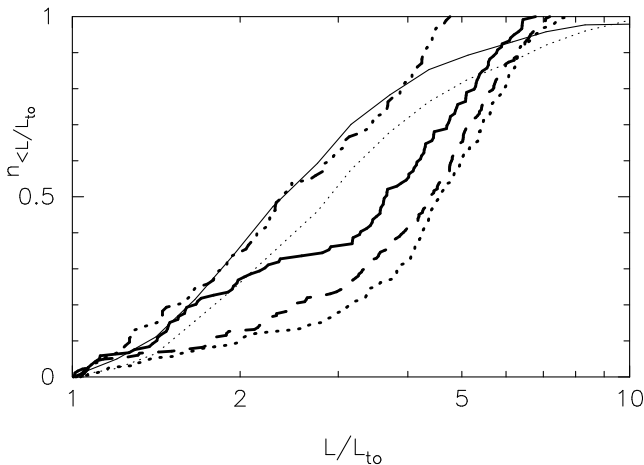


Figure 8. Cumulative distribution of L / L_{to} for simulations #1 (dotted curve), #2 (dashes), #3 (solid curve) and #4 (dash-3-dots). The thin solid and dotted curves show the cumulative distributions of the blue stragglers and bright ($M_v < -8.8$) and faint ($M_v > -8.8$) globular clusters, from the data of Piotto et al. (2004). The thin solid line appears to be consistent with the thick dash-3dotted curve, but bear in mind here that one is for a 100 Myr old population, whereas the other is for a 10 Gyr old population.

$m / m_{\text{to}} \simeq 1.4$ for simulation #4. As dynamical effects become more important (progressing from simulation #4 to #3, #2 and finally #1), the blue straggler luminosity distribution shifts to higher luminosities. This is a direct consequence of the changing importance of the main formation channels: binary evolution and stellar collisions. The latter channel is unimportant in low-density clusters, but dominates in the densest systems.

In our most compact model cluster, simulation #1, the majority of blue stragglers are the result of dynamical interactions—binary hardening and exchange—and tend to

be more massive than blue stragglers formed by binary evolution. Binary hardening boosts the number of blue stragglers by shifting the moment of Roche-lobe contact to an earlier evolutionary stage of the primary. In closer binaries, more of the donor mass can be transferred to the accretor without spillage, whereas in wider binaries most mass is lost from the binary system. Exchange interactions tend to substitute the lower mass binary component for a higher mass incoming star, with the result that post-encounter binary components tend to be more similar in mass than in the pre-encounter system. The binaries are generally also hardened in the process. Mass transfer in a binary consisting of two stars of comparable mass proceeds more conservatively than in unequal mass binaries. Thus, the higher encounter rate in denser systems has two distinct effects: it boosts the formation rate of blue stragglers, and also leads to more massive blue stragglers. However, we should bear in mind that, with $\lesssim 200$ blue stragglers present at any time during the first 100 Myr in our simulation models, their formation remains a rare event even in very dense clusters.

Overplotted in Figure 8 are two cumulative luminosity profiles from the observed sample of 2798 blue stragglers in 56 Galactic globular clusters from Piotto et al. (2004). They divided the clusters in which they found blue stragglers into two groups, one for “faint” clusters ($M_v > -8.8$; thin solid curve), the other for “bright” clusters ($M_v < -8.8$; thin dotted curve). The blue stragglers found in the denser clusters are typically brighter than those in the less dense clusters Piotto et al. (2004). The brightness distribution of the blue stragglers present at an age of 100 Myr in our simulation #4 is strikingly similar to the distribution of the observed blue stragglers in low density clusters, even though the ages are completely different (100 Myr for simulation #4, compared to about 10 Gyr for the globular cluster population). The main difference is at the high-luminosity end, which is in part a consequence of the larger relative brightness of the lower mass stars in the sample used by Piotto et al. (2004): at an age of 100 Myr, a star twice as massive as the turn-off is about an order of magnitude brighter than the turn-off luminosity, whereas at an age of 10 Gyr the luminosity difference is about a factor of 20.

In our simulation models #1–3 the number of collisions is probably much higher than in the old globular clusters used to compile the list of blue stragglers included in the thin dotted curve. The trend found by Piotto et al. (2004) that the blue stragglers formed in the more massive clusters are typically brighter is also present in our simulations. We find that clusters with a higher stellar density produce brighter blue stragglers. This is consistent with the expectation of Davies et al. (2004). In that case, we confirm that the higher encounter rate in the denser stellar environments contributes to the brighter blue stragglers.

Blue stragglers found in denser clusters are generally bluer than those in low density clusters (Piotto et al. 2004). This effect is also evident in Figure 9, which compares the temperatures and luminosities of the blue stragglers in simulations #1 and #4 at an age of 100 Myr. The denser model clusters tend to produce more massive and therefore bluer blue stragglers. We note that, even though all blue stragglers are (by definition) main-sequence stars, they have a broad range of temperatures for any given luminosity, because of the spread in their effective ages. The blue stragglers formed

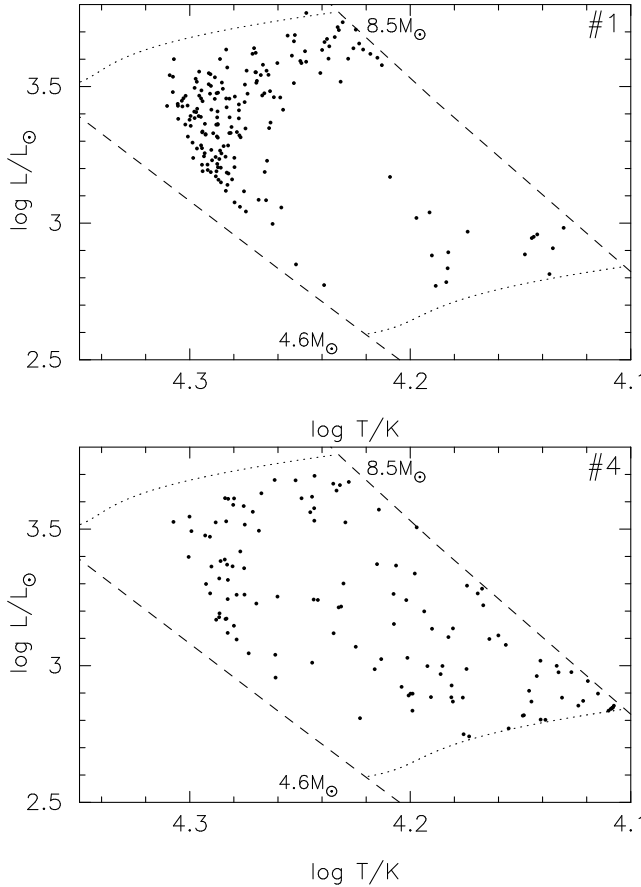


Figure 9. Temperatures and luminosities of the blue stragglers in simulations #1 and #4 at an age of 100 Myr. The two vertical dashed lines represent the zero-age main-sequence and the terminal age main-sequence. The two dotted curves are the main-sequence tracks for stars of $4.6 M_{\odot}$ (lower curve) and $8.5 M_{\odot}$ (upper curve).

in the densest clusters have the broadest range in ages, and are almost uniformly distributed between the zero-age and terminal-age main sequence.

3.5 Future blue stragglers

During the early evolution of our simulated clusters, a relatively large number of low-mass ($m \ll m_{\text{to}}$) stars receive mass from a companion star or participate in a merger. The resultant star will be rejuvenated, but so long as its mass lies below the turn-off it will not be identifiable as a blue straggler. Low-mass stars which accrete mass at an early stage appear as blue stragglers once the cluster has aged sufficiently to allow them to lag behind the main sequence turn-off. The early dynamical evolution of the cluster can thus lead to a reservoir of potential future blue stragglers, which become evident only later in the cluster's evolution. In each simulation, the number of such potential blue stragglers (specifically, rejuvenated main-sequence stars with $m < 4.6 M_{\odot}$, which corresponds to the turn-off mass at about 100 Myr, see § 3.2) was 250 ± 20 , where the error indicates the run-to-run variation. (We include here the additional constraint that a star must spend at least 10^5 years above the turn-off to be included.) The blue straggler mass distributions are

indistinguishable from one run to another: they are consistent with a constant number of potential blue stragglers per unit mass.

This lack of a trend in the properties of potential blue stragglers with cluster parameters is opposite to the trends seen in the actual blue stragglers identified during the first 100 Myr, where a clear dependence on cluster density is evident (see Figure 8). The reason is that most potential blue stragglers stem from evolving primordial binaries with relatively low-mass secondaries. Such binaries are not likely to be dynamically active, and their orbital parameters are largely unaffected by the dynamical evolution of the parent cluster. In our simulations, the secondary stars in binaries were initially distributed uniformly in mass between the minimum mass and the mass of the (pre-selected) primary (see § 2). The mass distribution of potential blue stragglers therefore simply follows the initial distribution of secondary masses.

The once dormant blue stragglers generally spend relatively little time as main-sequence stars above the turn off. Half (~ 120) live for less than 10 Myr, and fewer than 10% live between 30 Myr and 100 Myr as blue stragglers. Interestingly, the more massive stars ($\gtrsim 2.5 M_{\odot}$) tend to spend most time as blue stragglers. This can also be understood from binary evolution. Dormant blue stragglers in our runs are formed from mass transfer in primordial binaries of which the primary typically has $m > 4.6 M_{\odot}$. It is typically the secondary which eventually turns up as a blue straggler, and binaries with comparable component masses tend to produce the most massive blue stragglers. A very low-mass secondary will generally accrete little mass in a phase of mass transfer, resulting in a blue straggler that spends only a short time above the turn-off, and never very far above it. A star is rejuvenated more effectively when it has accreted more mass and when it is evolved further along its main sequence, both effects resulting in a longer blue straggler lifetime.

3.6 OB runaway stars

The Galaxy contains a population of stars having velocities $> 40 \text{ km s}^{-1}$. These objects are generally called OB runaways (Blaauw & Morgan 1954; Blaauw 1993), because of their high velocities and predominant spectral type. There are two main theories to explain these high velocity objects: ejection from a binary system as the companion experiences a supernova, and dynamical ejection following a close multi-body encounter (Leonard 1995). The first mechanism was studied extensively by means of binary evolution of individual cases (van Rensbergen et al. 1996) and by synthesizing entire Galactic binary populations (Portegies Zwart 2000). The dynamical ejection mechanism has attracted considerable attention in the past few years, and has been studied for individual cases (Gualandris et al. 2004) and in population studies (Leonard 1995). Neither theory satisfactorily explains the origin of most runaways.

From an observational point of view, both scenarios seem to operate concurrently. A large number of supernova-produced runaways were identified by Hoogerwerf et al. (2000) using the Hipparcos database, and individual cases were also revealed to originate from this scenario (Kaper et al. 1997), but some clear cases must have their

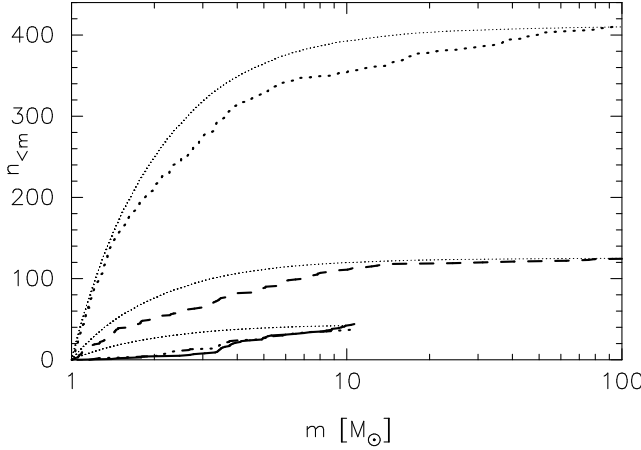


Figure 10. Cumulative mass distribution of runaway stars ($v > 40 \text{ km s}^{-1}$) for simulations #1 (dotted curve, 444 stars), #2, (dashes, 131 stars) and (combined) models #3 and #4 (dash-dot curve, 46 and 38 stars, respectively). The Salpeter initial mass function used as initial conditions for the simulations is presented as the thin solid curve. Only stars which escape within 100 Myr with velocity exceeding 40 km/s are shown.

origin in dynamical ejection (Gies & Bolton 1986). Clearly, the jury is still out on the mechanism responsible for OB runaway stars. The majority of runaways are high-mass stars. Furthermore, some 40% of all stars of spectral type O are runaways, and 25% of all B stars, but only 4% of A stars (Blaauw & Morgan 1954; Blaauw 1993).

In our simulations we encountered quite a number of ejected stars having velocities high enough for them to be considered runaways. Within 100 Myr, a total of 6950 ± 150 stars were ejected from each cluster. The number of stars ejected at high speed does not seem to depend on the initial cluster density. The denser clusters, however, do tend to eject more main-sequence stars and at an earlier age, while less concentrated clusters tend to eject more white dwarfs. In simulation #1, a total of 815 main-sequence stars were ejected with high ($> 40 \text{ km s}^{-1}$) velocity, compared to 290 from simulation #2, 103 from #3 and 67 from simulation #4. The number of ejected high-speed binaries tends to increase with cluster density, from about 150 for the shallowest cluster (#4) to about 200 for the most concentrated model (#1). Only 2–3% of the ejected stars are members of binaries, whereas the overall binary fraction initially is 10%.

At zero age, our models contained 2695 stars of spectral type O9.5 or earlier. With a total of 444 runaways in simulation #1, including less than 100 O stars, we find fewer than 4% runaways among the spectral type O stars. Thus it seems that even in the densest clusters OB runaways are underproduced by about an order of magnitude compared to observations. Note in addition that the runaways on average spend about 60–80% of their main-sequence lifetimes in the cluster before acquiring high velocities, so the discrepancy with the observations is actually even larger. Lower mass stars tend to spend more time in the cluster before they are ejected. The fraction of binaries among the OB runaways is 12%, considerably higher than the overall binary fraction among ejected stars, and comparable to the initial binary fraction.

Figure 10 shows the cumulative mass distribution of

stars which escaped our simulated clusters with velocities exceeding 40 km s^{-1} . For comparison we also plot the adopted Salpeter initial mass function (thin solid curve). Evidently, the mass distribution of runaway stars from the most concentrated clusters tends to follow the initial mass function in these models, while shallower models contain a much greater proportion of high-mass stars.

The ejection of compact objects was discussed in § 3.7, but in our simulations a sizable number of massive stars are ejected before exploding as supernovae. These high-velocity stars will therefore produce supernovae in the interstellar medium. For simulated clusters #1, #2, #3 and #4, respectively, a total of 78, 26, 10 and 4 stars with $m > 8 M_\odot$ were ejected before becoming supernovae. In simulation #1, half (40) of these travel a distance of $\sim 0.5 \text{ kpc}$ before exploding; the maximum distance was 4.4 kpc.

3.7 Evolution of compact objects

Black holes and neutron stars receive kicks upon formation in our simulations. These natal kicks can be quite high (Dewey & Cordes 1987; Lyne & Lorimer 1994; Wang et al. 2006) and we select them (with random direction) from a Paczynski-Hartman distribution (Paczynski 1990; Hartman 1997), which has a dispersion of $\sigma_{\text{kick}} = 300 \text{ km s}^{-1}$. Black holes seem to receive on average lower kicks (White & van Paradijs 1996; Gualandris et al. 2005), and in our simulations a black hole of mass m_{bh} receives a kick drawn from the same distribution as the neutron star kicks, but reduced by a factor of $1.4 M_\odot/m_{\text{bh}}$.

Table 2 presents the number of core collapse supernovae and compact objects produced for the simulations listed in Table 1. In each run, about 1700 black holes form in Type Ic supernovae, and 6500 neutron stars form in Type Ib or Type II supernovae. Although the various models share the same realization of the initial mass function, the numbers of supernovae differ slightly from run to run; with more supernovae occurring in the larger, less dense clusters. This is caused mainly by variations in binary evolution, due to the differences in binary separations and cluster density between runs. Also, for individual supernovae the kick is applied randomly, with different random seeds for different runs. This introduces an unbiased variation in the evolution of the massive binary population, giving rise to additional slight differences in the numbers of compact objects that remain bound to their parent cluster.

The lower kicks imparted to black holes mean that a smaller fraction of them escape the cluster. The retention fraction for black holes ranges from 0.48 to 0.71 (see Table 2); for neutron stars, the range is 0.065 to 0.12. The densest clusters retain most compact objects, because of their larger escape speeds. The range of retention fraction is about a factor of two, while the densest cluster has an escape velocity roughly four times greater than that of the least dense cluster.

Most compact objects are single, since supernovae are very effective at destroying binaries. At an age of 100 Myr, only about 4% of black holes and $\sim 2\%$ of neutron stars are members of binary systems. These fractions are lower than the overall binary fraction ($\sim 10\%$) mainly due to evolution of the binary companion, and also because of differences in the amount of mass lost during the supernova—the formation

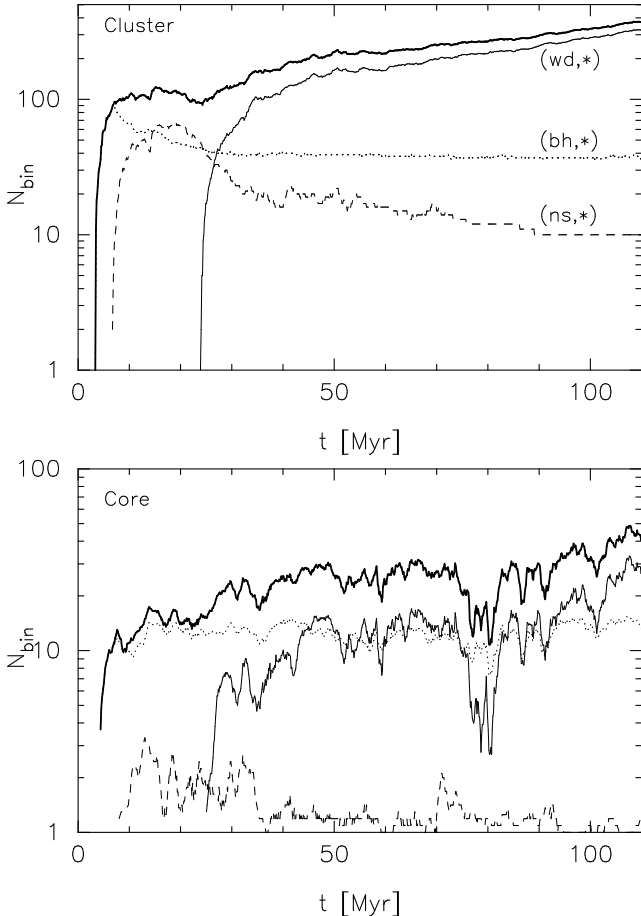


Figure 11. Number of binaries containing a compact object as a function of time for simulation #2. The upper panel presents data for the entire cluster, whereas the lower panel includes only binaries within $2r_{\text{core}}$. In each panel, the top (thick solid) curve gives the total number of binaries containing at least one compact object (bh, ns or wd). The thin solid curve gives the number of binaries containing one white dwarf, dashes are for neutron stars, and dots are for binaries containing at least one black hole. Note that due to double counting the total of the thin curves does not add up to the thick curve.

of a neutron star is generally associated with considerably more mass loss than is the creation of a black hole. The companion of a black hole is generally rather massive and may also explode in a supernova to form another black hole or a neutron star, but only a few binaries survive both supernovae. No binary containing two neutron stars was formed in any of our simulations, whereas black holes tend to be paired with other black holes (see Table 2).

Black holes are also more likely than neutron stars to have a main sequence star or a giant as a companion. Most of these binaries, indicated by (bh,ms) in Table 2, will become X-ray binaries at some point during their evolution. Among these binaries, black-hole accretors are about twice as common as neutron-star accretors. We therefore expect that in star clusters with ages ~ 100 Myr, X-ray binaries containing a black hole may be quite common, possibly even more common than X-ray binaries with a neutron star.

Figure 11 presents, for simulation #2, the numbers of binaries containing at least one compact object, as func-

tions of time. The number of black holes in binaries rises sharply shortly after the start of the simulation, with a peak at around 8 Myr. This is the moment when the turn-off mass drops below the minimum mass for forming black holes ($\sim 23 M_{\odot}$), and lower mass stars form neutron stars. The number of black holes in binaries drops rapidly from this moment on because many of their companions form neutron stars in supernova explosions (see Table 2). This transition is also visible in the sharp increase at 8 Myr of the number of binaries containing a neutron star. Note that binaries containing a neutron star and a black hole are counted twice in this figure, as both (bh, \star) and (ns, \star).

White dwarfs become significant components of the compact binary population after about 25 Myr, at a turn-off mass of about $10 M_{\odot}$. Stars of $\lesssim 8 M_{\odot}$ evolving in isolation turn into white dwarfs, but in a binary system early stripping of the hydrogen envelope may cause a more massive star to become a white dwarf instead of collapsing to a neutron star. The population of compact binaries in clusters older than about 40 Myr is dominated by white dwarfs. The naked cores of stars which are stripped of their hydrogen envelope, exposing their hot helium interior, are also included in this category, but Wolf-Rayet stars are not. The reverse process may also occur: If a sufficient amount of mass is accreted by (say) a $7 M_{\odot}$ star it may, by the end of its fuel processing life, still collapse to a neutron star in a supernova explosion, whereas under normal circumstances it would become a white dwarf. A similar process may result in the formation of a black hole from a star of mass $\lesssim 23 M_{\odot}$.

One interesting evolutionary product of such a process is a binary in which a neutron star is accompanied by a white dwarf in an eccentric orbit. Such a population, predicted by binary population synthesis models (Portegies Zwart & Yungelson 1999), seems to be quite common in our simulations. Although the statistics are poor, approximately half (18 of 32) of our (ns, wd) binaries have quite high eccentricities: $e = 0.45 \pm 0.27$. In only one of these cases (in simulation #1) was the eccentricity induced by a strong dynamical encounter with another cluster member; in all others it was the result of reverse evolution, as described by Portegies Zwart & Yungelson (1999): For sufficiently massive binaries (with a $\gtrsim 8 M_{\odot}$ secondary), mass transfer can result in a reversal of the order in which the component stars become supernova (Pols 1994), causing the less massive (secondary) star to explode before the primary. If the mass of the secondary star is just below the limit for forming a black hole, such a reversal in the supernova order may lead to binaries with a mildly recycled millisecond pulsar orbiting a black hole (Sipior et al. 2004). In our simulations we find a total of 5 such cases out of 19 binaries in which a black hole is accompanied by a normal radio pulsar, much larger than predicted from the simulations of (Sipior et al. 2004). The difference in formation rate stems in large part from differences in initial conditions. The maximum initial separation in our simulations was chosen based on the hard-soft boundary (Heggie 1975) for that particular cluster, whereas Sipior et al. adopted a maximum separation based on observed binaries in the solar neighborhood.

Table 2. Some characteristics of the compact object population at 100Myr. The first column identifies the run, followed by the total number of core collapse supernovae that result a black hole (Ic) or a neutron star (Ib+II). The next two columns give the number of black holes and neutron stars still present in the cluster at an age of 100 Myr. The following columns give the number of binaries containing two black holes (bh,bh), a black hole and a neutron star (bh,ns), or a white dwarf (bh,wd) and (ns,wd). The final two columns give the number of black holes and neutron stars that are accompanied by a main-sequence star; note that the few that are accompanied by an evolved giant star are also included in this category.

Simulation	Ic	Ib+II	N_{bh}	N_{ns}	(bh,bh)	(bh,ns)	(bh, wd)	(ns, wd)	(bh, ms)	(ns, ms)
#1R	1632	6520	1152	811	14	8	1	7	10	13
#1	1656	6584	1017	585	12	1	1	7	13	5
#2	1710	6446	1028	553	16	4	7	5	10	1
#3	1717	6387	834	365	17	2	9	4	9	3
#4	1728	6735	828	436	11	4	5	9	13	5

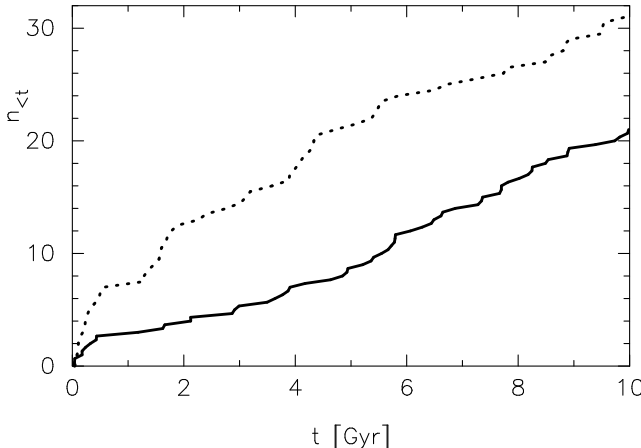


Figure 12. Cumulative distribution of merger times for (wd, wd) binaries for the compact clusters #1 and #2 (solid curve) and for the shallow clusters #3 and #4. These distributions were created from the cluster populations at an age of 100 Myr.

3.8 Gravitational wave sources and type Ia supernovae

The compact object binaries in our simulated clusters may at some time become sources of gravitational waves. The binaries containing back holes or neutron stars are not very promising gravitational wave sources because they are rare (see however Kocsis et al. (2006)), but a sizable fraction of binaries with two white dwarfs may become important sources for space-based gravitational wave detectors (Nelemans et al. 2004; Stroeer et al. 2005). In order to improve the statistics we combine the white dwarf binaries formed in simulations #1R, #1 and #2, and those in simulations #3 and #4. The total number of white dwarf binaries that engage in Roche-lobe overflow within 10 Gyr is 21 ± 2 per cluster in the denser clusters (#1 and #2), and 31 ± 1 in the shallower clusters (#3 and #4).

Figure 12 shows the cumulative distributions of merger times for those double degenerate binaries that merge within 10 Gyr. The double degenerates in the concentrated clusters (#1 and #2) have an average merger time of 5.2 ± 2.5 Gyr, compared to 3.7 ± 2.6 Gyr for those in the shallower clusters. Thus, more concentrated clusters tend to produce fewer double degenerate binaries, with somewhat longer merger times. This is probably related to the tendency of the more con-

centrated clusters to contain more binaries with shorter orbital period and more comparable component masses. Both effects are mediated by the higher interaction rates in the denser clusters (see § 3.4, where this effect is discussed in relation to the formation of blue stragglers).

The reduced formation rate of merging white-dwarf binaries (the potential sources of Type Ia supernovae) in the densest clusters contrasts with the earlier findings of Shara & Hurley (2002), who found a ten-fold enhancement of the merger rate. However, the results are hard to compare, as the initial conditions are quite different, as are the effective time frames over which the simulations are performed.

According to the binary population synthesis calculations of Nelemans et al. (2001), the Galaxy contains about 1.1×10^8 (wd, wd) binaries, giving rise to a merger rate of 0.011 per year. Correcting this merger rate for initial conditions of the primordial binary population adopted in our simulations, we find $\sim 5 \times 10^6$ (wd, wd) mergers during a Hubble time in the Galaxy, consistent with the predicted merger rate of simulation models #3 and #4 if we simply assume that all stars in the Galaxy formed in such clusters. The distribution of mergers for these two models is presented as the dotted line in Figure 12, which has roughly equal probability per unit time. For the densest clusters (simulations #1 and #2), however, the population of (wd, wd) binaries that merge in a Hubble time is smaller by about one-third. Binaries that favor blue straggler formation (see § 3.4) generally do not produce short-period (wd, wd) binaries.

In the more concentrated clusters, the mean mass for the most massive white dwarf in a binary is $\langle m \rangle = 1.23 \pm 0.03 M_{\odot}$, with a mass ratio of $\langle q \rangle = 0.87 \pm 0.07$ (see Figure 13). For the shallower clusters, the distributions in mass and mass ratio are much broader, but have similar means: $\langle m \rangle = 1.21 \pm 0.09 M_{\odot}$, $\langle q \rangle = 0.84 \pm 0.08$. We note here that the potential merging white dwarf binaries in the simulations of Shara & Hurley (2002) have $\langle q \rangle = 0.69 \pm 0.18$, considerably smaller than the value found here. However, differences in the cluster age have a substantial effect on the final mass ratio, in the sense that, in older star clusters like those of Shara & Hurley (2002), the secondary white dwarfs tend to be of lower mass.

The distributions of primary and secondary masses in double degenerate binaries are presented in Figure 13. The primary mass white dwarfs in the denser clusters tend to cluster around $1.23 M_{\odot}$. The majority of these white dwarfs are formed following stable mass transfer from an

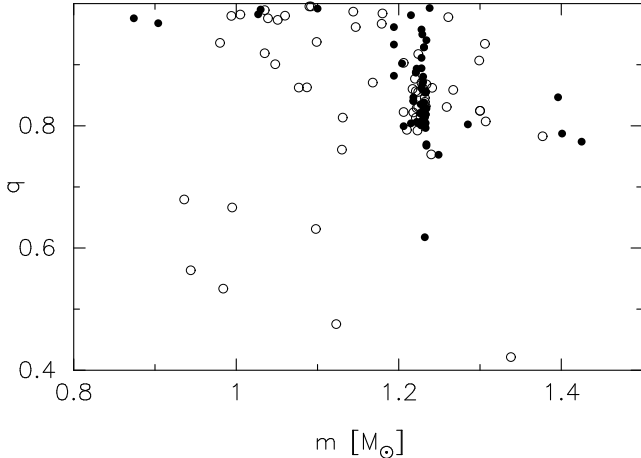


Figure 13. Distribution of primary mass versus mass ratio in (wd, wd) binaries at an age of 100 Myr for the concentrated clusters #1 and #2 (bullets) and the shallow clusters #3 and #4 (open circles).

$\sim 8-12 M_{\odot}$ star. This can only happen in case A mass transfer (Kippenhahn & Weigert 1967), i.e., in a short-period binary. Denser clusters tend to produce more such systems, as dynamical hardening of the binary reduces the orbital period, favoring stable mass transfer. The consequences of such reversed evolution were discussed in § 3.7.

The larger number of dynamical encounters in the denser star clusters leads to much narrower distributions in both primary mass and mass ratio compared to the shallower clusters. Interactions tend to put the most massive stars into tighter binaries, and the combination of tighter binaries and more massive companions, tends to cause mass transfer in mass-transferring binaries to be more conservative. As a consequence, the resultant white dwarfs are more massive. By the end of our simulations (at 100 Myr), only about 6% of stars have evolved into white dwarfs (see Figure 5), whereas at 10 Gyr every star will be a remnant (for our initial mass function), so the population of binary white dwarfs is still expected to change quite substantially. However, the majority of massive white dwarfs in relatively tight binaries, which are the most promising sources of type Ia supernovae, and which are also easiest to observe by gravitational wave observatories, form during the first 100 Myr.

4 CONCLUSIONS

We have simulated star clusters with highly concentrated initial density profiles and a wide range of initial relaxation times, from birth to an age of about 100 Myr. Our initial conditions include 10% hard primordial binaries, and the simulations incorporate the effects of stellar and binary evolution and binary dynamics.

In this second paper on these simulations, we report on the time variation of the structural and internal composition parameters describing our model clusters, and compare our results directly to the sample of relatively young and isolated star clusters in the Large Magellanic Cloud. On the basis of this comparison, we conclude that the range of core radii and concentrations found in our simulated clusters is

consistent with observations of the LMC clusters, and we argue that most of the LMC clusters are born with initial half-mass relaxation times of 200 Myr to 600 Myr and high central concentrations— $c \simeq 2.7$ (King parameter $W_0 \simeq 12$). The only clear exception to this is the star cluster R 136 in the 30 Doradus region, which matches our simulation with an initial relaxation time of about 80 Myr.

Due to mass segregation, the mass function of intermediate-mass main-sequence stars becomes as flat as $\alpha = -1.8$ in the central part of the cluster (where the initial Salpeter mass function had $\alpha = -2.35$). In the outer regions, the mass function exponent is as steep as $\alpha = -2.6$. By the end of the simulations, at 100 Myr, the overall cluster binary fraction is still $\sim 10\%$, but in the core the fraction of binaries is somewhat higher ($\gtrsim 12\%$). By this time about 7% of the single stars are remnants, and their number is increasing gradually at a rate of about 0.1% per Myr.

In our simulations a large number of blue stragglers are formed. At any time, however, no more than 100–200 blue stragglers are visible in the cluster. The largest numbers of blue stragglers are formed in the densest clusters. The distribution of blue straggler masses depends quite sensitively on the initial cluster density. The densest clusters tend to produce more massive, brighter and bluer blue stragglers than less dense clusters. The trends visible in our simulations are consistent with observations of current globular clusters. A population of dormant blue stragglers is formed early in the evolution of the cluster. They remain hidden on the main-sequence until they emerge hidden above the turn-off as the cluster ages.

The fraction of high-velocity stars of spectral type O and B is considerably smaller than the fractions observed in the Galactic field. Our simulations, however, incorporate both of the effects thought to be responsible for the acceleration of the observed OB runaways: supernova in evolving binaries and gravitational slingshots from multi-body scattering encounters. The discrepancy with observations of the numbers of OB runaways might conceivably be explained by the initial binary fraction, which in our simulations is only 10%.

Shortly after formation, the cores of our simulated clusters become quite rich in compact stars. Up to an age of about 40 Myr the remnant population in cluster cores is dominated by stellar-mass black holes; after that time white dwarfs take over. Neutron stars are easily ejected from the clusters and there are only a few present at any time. The neutron star retention fraction is about 6–12%, whereas 50–70% of black holes are retained. Clusters with longer relaxation times have smaller retention fractions. Binaries containing black holes with main-sequence companions outnumber those containing a neutron star and a stellar companion. We conclude that these clusters may be relatively rich in x-ray binaries with a black hole as accreting object, at least up to ages of a few hundred Myr.

Binaries containing two white dwarfs are quite common in our simulations, and 20–30 have sufficiently small orbital periods that gravitational radiation will bring the two white dwarfs into contact within a Hubble time. Interestingly, clusters with shorter relaxation time produce systematically fewer white-dwarf binaries that will merge within a Hubble time.

ACKNOWLEDGMENTS

We are grateful to Douglas Heggie and Piet Hut for discussions. SPZ and SMcM thank Tokyo University for the use of their GRAPE-6 hardware. The calculations were performed on the MODESTA GRAPE-6 systems in Amsterdam and the GRAPE-6 platform at Drexel University. This research was supported in part by the Netherlands Organization for Scientific Research (NWO grant No. 635.000.001 and 643.200.503), the Netherlands Advanced School for Astronomy (NOVA), the Royal Netherlands for Arts and Sciences (KNAW), the Leids Kerkhoven-Bosscha fonds (LKBF) by NASA ATP grant NNG04GL50G. Parts of the manuscript were completed during a visit (by SPZ and SLWM) to the Kavli Institute for Theoretical Physics at UC Santa Barbara, supported in part by the National Science Foundation under Grant No. PHY99-07949.

REFERENCES

Bate, M. R., Bonnell, I. A. 2005, *MNRAS*, 356, 1201
 Bica, E., Dutra, C. M., Barbuy, B. 2003a, *A&A*, 397, 177
 Bica, E., Dutra, C. M., Soares, J., Barbuy, B. 2003b, *A&A*, 404, 223
 Blaauw, A. 1993, in *ASP Conf. Ser.* 35: Massive Stars: Their Lives in the Interstellar Medium, 207
 Blaauw, A., Morgan, W. W. 1954, *ApJ*, 119, 625
 Casertano, S., Hut, P. 1985, *ApJ*, 298, 80
 Clark, J. S., Negueruela, I., Crowther, P. A., Goodwin, S. P. 2005, *A&A*, 434, 949
 Davies, M. B., Piotto, G., de Angeli, F. 2004, *MNRAS*, 349, 129
 Dewey, R. J., Cordes, J. M. 1987, *ApJ*, 321, 780
 Eggleton, P. P., Fitchett, M. J., Tout, C. A. 1989, *ApJ*, 347, 998
 Figer, D. F. 2005, *Nat*, 434, 192
 Figer, D. F., MacKenty, J. W., Robberto, M., Smith, K., Najarro, F., Kudritzki, R. P., Herrero, A. 2006, *ApJ*, 643, 1166
 Figer, D. F., McLean, I. S., Morris, M. 1999, *ApJ*, 514, 202
 Figer, D. F., Najarro, F., Gilmore, D., Morris, M., Kim, S. S., Serabyn, E., McLean, I. S., Gilbert, A. M., Graham, J. R., Larkin, J. E., Levenson, N. A., Teplitz, H. I. 2002, *ApJ*, 581, 258
 Freitag, M., Gürkan, M. A., Rasio, F. A. 2006, *MNRAS*, 368, 141
 Genzel, R., Schödel, R., Ott, T., Eisenhauer, F., Hofmann, R., Lehnert, M., Eckart, A., Alexander, T., Sternberg, A., Lenzen, R., Clénet, Y., Lacombe, F., Rouan, D., Renzini, A., Tacconi-Garman, L. E. 2003, *ApJ*, 594, 812
 Ghez, A. M., Duchêne, G., Matthews, K., Hornstein, S. D., Tanner, A., Larkin, J., Morris, M., Becklin, E. E., Salim, S., Kremenek, T., Thompson, D., Soifer, B. T., Neugebauer, G., McLean, I. 2003, *ApJL*, 586, L127
 Gies, D. R., Bolton, C. T. 1986, *ApJS*, 61, 419
 Gualandris, A., Colpi, M., Portegies Zwart, S., Possenti, A. 2005, *ApJ*, 618, 845
 Gualandris, A., Portegies Zwart, S., Eggleton, P. P. 2004, *MNRAS*, 350, 615
 Gürkan, M. A., Freitag, M., Rasio, F. A. 2004, *ApJ*, 604, 632
 Hartman, J. W. 1997, *A&A*, 322, 127
 Heggie, D. C. 1975, *MNRAS*, 173, 729
 Heggie, D. C., Mathieu, R. 1986, *MNRAS*, in P. Hut, S. McMillan (eds.), *Lecture Not. Phys* 267, Springer-Verlag, Berlin
 Heggie, D. C., Trenti, M., Hut, P. 2006, *ArXiv Astrophysics e-prints*
 Hoogerwerf, R., de Bruijne, J. H. J., de Zeeuw, P. T. 2000, in Accepted for publication in the *A&A*. 29 pages, 19 figures, 10057
 Hurley, J. R., Tout, C. A., Aarseth, S. J., Pols, O. R. 2001, *MNRAS*, 323, 630
 Hut, P., Shara, M. M., Aarseth, S. J., Klessen, R. S., Lombardi, Jr., J. C., Makino, J., McMillan, S., Pols, O. R., Teuben, P. J., Webbink, R. F. 2003, *New Astronomy*, 8, 337
 Kaper, L., van Loon, J. T., Augusteijn, T., Goudfrooij, P., Patat, F., Waters, L. B. F. M., Zijlstra, A. A. 1997, *ApJL*, 475, L37
 King, I. R. 1966, *AJ*, 71, 64
 Kippenhahn, R., Weigert, A. 1967, *Zeitschr. f. Astroph.*, 65, 251
 Klessen, R. S. 2001, *ApJ*, 556, 837
 Kocsis, B., Gaspar, M. E., Marka, S. 2006, *ArXiv Astrophysics e-prints*
 Kroupa, P. 2001, *MNRAS*, 322, 231
 Lamers, H. J. G. L. M., Anders, P., de Grijs, R. 2006, *A&A*, 452, 131
 Leonard, P. J. T. 1995, *MNRAS*, 277, 1080
 Lombardi, J. C., Thrall, A. P., Deneva, J. S., Fleming, S. W., Grabowski, P. E. 2003, *MNRAS*, 345, 762
 Lombardi, Jr., J. C., Warren, J. S., Rasio, F. A., Sills, A., Warren, A. R. 2002, *ApJ*, 568, 939
 Lyne, A. G., Lorimer, D. R. 1994, *Nat*, 369, 127+
 Mackey, A. D., Gilmore, G. F. 2003, *MNRAS*, 338, 85
 Makino, J., Fukushige, T., Koga, M., Namura, K. 2003, *Publ. Astr. Soc. Japan*, 55, 1163
 Makino, J., Taiji, M., Ebisuzaki, T., Sugimoto, D. 1997, *ApJ*, 480, 432
 Massey, P., Hunter, D. A. 1998, *ApJ*, 493, 180
 McCrady, N., Gilbert, A. M., Graham, J. R. 2003, *ApJ*, 596, 240
 Merritt, D., Piatek, S., Portegies Zwart, S. P., Hemsendorf, M. 2004, *ApJL*, 608, L25
 Moffat, A. F. J., Drissen, L., Shara, M. M. 1994, *ApJ*, 436, 183
 Moffat, A. F. J., Poitras, V., Marchenko, S. V., Shara, M. M., Zurek, D. R., Bergeron, E., Antokhina, E. A. 2004, *AJ*, 128, 2854
 Nelemans, G., Yungelson, L. R., Portegies Zwart, S. F. 2001, *A&A*, 375, 890
 Nelemans, G., Yungelson, L. R., Portegies Zwart, S. F. 2004, *MNRAS*, 349, 181
 Paczynski, B. 1990, *ApJ*, 348, 485
 Padoan, P., Nordlund, Å. 2002, *ApJ*, 576, 870
 Piatti, A. E., Bica, E., Claria, J. J. 1998, *A&AS*, 127, 423
 Piotto, G., De Angeli, F., King, I. R., Djorgovski, S. G., Bono, G., Cassisi, S., Meylan, G., Recio-Blanco, A., Rich, R. M., Davies, M. B. 2004, *ApJL*, 604, L109
 Pols, O. R. 1994, *A&A*, 290, 119
 Pols, O. R., Marinus, M. 1994, *A&A*, 288, 475
 Portegies Zwart, S. F. 2000, *ApJ*, 544, 437

Portegies Zwart, S. F., Baumgardt, H., Hut, P., Makino, J., McMillan, S. L. W. 2004, *Nat* , 428, 724

Portegies Zwart, S. F., Hut, P., McMillan, S. L. W., Verbunt, F. 1997, *A&A* , 328, 143

Portegies Zwart, S. F., Makino, J., McMillan, S. L. W., Hut, P. 1999, *A&A* , 348, 117

Portegies Zwart, S. F., McMillan, S. L. W. 2002, *ApJ* , 576, 899

Portegies Zwart, S. F., McMillan, S. L. W., Hut, P., Makino, J. 2001, *MNRAS* , 321, 199

Portegies Zwart, S. F., Verbunt, F. 1996, *A&A* , 309, 179

Portegies Zwart, S. F., Yungelson, L. R. 1998, *A&A* , 332, 173

Portegies Zwart, S. F., Yungelson, L. R. 1999, *MNRAS* , 309, 26

Salpeter, E. E. 1955, *ApJ* , 121, 161

Shara, M. M., Hurley, J. R. 2002, *ApJ* , 571, 830

Shara, M. M., Hurley, J. R. 2006, *ApJ* , 646, 464

Sills, A., Adams, T., Davies, M. B. 2005, *MNRAS* , 358, 716

Sills, A., Deiters, S., Eggleton, P., Freitag, M., Giersz, M., Heggie, D., Hurley, J., Hut, P., Ivanova, N., Klessen, R. S., Kroupa, P., Lombardi, J. C., McMillan, S., Portegies Zwart, S. F., Zinnecker, H. 2003, *New Astronomy*, 8, 605

Sills, A., Faber, J. A., Lombardi, Jr., J. C., Rasio, F. A., Warren, A. R. 2001, *ApJ* , 548, 323

Sills, A., Lombardi, J. C. 1997, *ApJL* , 484, L51

Sipior, M. S., Portegies Zwart, S., Nelemans, G. 2004, *MNRAS* , 354, L49

Smith, L. J., Gallagher, J. S. 2001, *MNRAS* , 326, 1027

Stolte, A., Brandner, W., Grebel, E. K., Lenzen, R., Lagrange, A.-M. 2005, *ApJL* , 628, L113

Stroeer, A., Vecchio, A., Nelemans, G. 2005, *ApJL* , 633, L33

Takahashi, K., Portegies Zwart, S. F. 2000, *ApJ* , 535, 759

Trenti, M., Heggie, D. C., Hut, P. 2006, *ArXiv Astrophysics e-prints*

van Rensbergen, W., Vanbeveren, D., de Loore, C. 1996, *A&A* , 305, 825

Wang, C., Lai, D., Han, J. L. 2006, *ApJ* , 639, 1007

Weidner, C., Kroupa, P. 2004, *MNRAS* , 348, 187

White, N. E., van Paradijs, J. 1996, *ApJL* , 473, L25+

